Identification of Near-Earth Asteroids Using Multi-Spacecraft Systems

Heiligers, M.J.; Guo, J.; Vermeulen, J.G.P.

Publication date
2022

Published in
Proceedings of the International Astronautical Congress

73rd International Astronautical Congress (IAC), Paris, France, 18-22 September 2022.

IAC-22,E10,1,9,x69394

Identification of Near-Earth Asteroids Using Multi-Spacecraft Systems

Arjan Vermeulen[a]*, Jian Guo[b] and Jeannette Heiligers[c]

[a] *Master student, TU Delft Faculty of Aerospace Engineering, Kluyverweg 1, Delft, The Netherlands*
[b] *Associate Professor, TU Delft Faculty of Aerospace Engineering, Kluyverweg 1, Delft, The Netherlands*
[c] *Assistant Professor, TU Delft Faculty of Aerospace Engineering, Kluyverweg 1, Delft, The Netherlands*
* Corresponding Author

Abstract

Through numerous survey efforts over the past decades, humanity has achieved substantial knowledge of the near-Earth asteroid (NEA) population. Nevertheless, survey completeness at small asteroid sizes is still limited, and unannounced impacts, such as the 2013 Chelyabinsk meteor, are common enough to warrant further identification efforts. Because of the limitations of Earth-based surveys, several works have already investigated an NEA cataloguing survey from deep space using a single spacecraft. An extension to this idea is proposed, where a multi-spacecraft system in orbit around the Sun is utilized to perform such a survey. This offers several distinct advantages over a single spacecraft system, such as a decrease in blind spots due to Solar interference, faster asteroid orbit determination through triangulation, and the possibility for more advanced search strategies. A survey simulation tool was developed to predict the expected survey completeness for a range of design parameters of the survey using a sample population of NEAs. Investigated parameters include the number of spacecraft; their payload, either visual light or thermal infrared telescopes; and the semi-major axis, eccentricity and mean anomaly of their heliocentric orbits. At each timestep in the five-year simulation, the tool calculates the target and background signal from each asteroid to each spacecraft. From these, the signal-to-noise ratio is determined which is used in a probabilistic detection model. Lastly, if sufficient detections are established in a 90-day period, the asteroid is labelled as identified. Initially, co-orbital configurations of spacecraft are studied, where all spacecraft are located in the same orbit, but spread apart. It is found that a circular orbit with the spacecraft distributed evenly across the orbit provides the best results and that thermal infrared telescopes outperform visual light telescopes in all conditions. The optimal semi-major axis increases with increasing number of spacecraft, starting at 0.9AU for a single spacecraft, increasing by 0.03AU per additional spacecraft. The findings are supported by a novel hypothesis that relates the expected survey completeness to the volume of space in which NEAs at varying limiting magnitudes can be effectively detected. Non-co-orbital arrangements are investigated using a preliminary Bayesian optimization process and so far indicate no significant performance increase compared to the co-orbital configurations. As a general conclusion, performance predictions indicate that a multi-spacecraft system of 2-3 spacecraft will identify 40-60% more NEAs than a single spacecraft, with strong diminishing returns for larger numbers of spacecraft.

Keywords: Near-Earth asteroids, multi-spacecraft systems, detection, identification

1. Introduction

Asteroid impacts present one of the rarest, and least predictable, natural disasters known to humanity. Since the discovery that the non-avian dinosaurs went extinct due to the Chixculub impact 66 million years ago, humanity has undertaken significant effort to guard itself from this extra-terrestrial threat. For this reason, it is perhaps surprising that our knowledge of the NEA population is very limited. The Spaceguard survey effort started in the 1990s set a goal of identifying 90% of NEAs over 140 m in diameter [1], and although this goal will be met very soon, smaller NEAs are still largely unknown.

Figure 1 shows the identification completeness as a function of asteroid size: most, if not all NEAs of similar size to the Chixculub impactor have been identified [3]. However, most NEAs of a few tens of meters in size still remain unidentified.

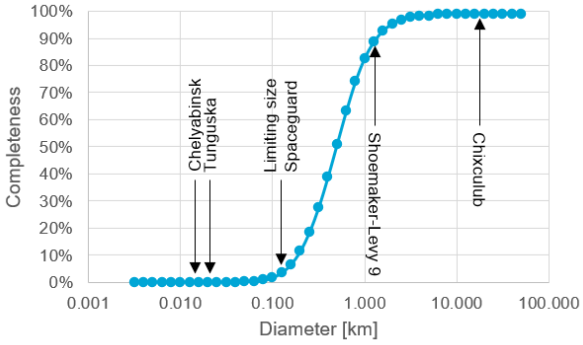

Figure 1: Survey completeness as a function of asteroid diameter. [2]

Although small, these objects still pose a threat, as was illustrated by the Chelyabinsk event in 2013. Detection

of these very small objects is difficult from Earth due to interference of the atmosphere, and therefore detection from space might be preferred [4]. Some recent missions, most notably the NEOWISE mission, have successfully identified large quantities of small NEAs from Earth orbit [5]. However, interference from radiation from Earth and the Moon is detrimental to performance [4], and NEAs on an impact trajectory might not be detected if they approach Earth from the direction of the Sun: for example, the NEA which entered the atmosphere over Chelyabinsk in 2013 remained completely undetected until atmospheric entry [6].

In recent years, several authors (e.g. Stokes et al. [4], Ramirez Torralba and Heiligers [6]) have already proposed conducting NEA surveys from deep space. This allows detection of NEAs away from the interference of the Earth and Moon, as well as detecting NEAs approaching Earth along the Sun-Earth line. Stokes et al. [4] studied singular spacecraft in orbit around Earth or Venus, while Ramirez Torralba and Heiligers [6] investigated using spacecraft in various orbits around the Sun-Earth and Sun-Venus Lagrange points. In this work, the position, composition, and performance of a multi-spacecraft system is investigated in a more generic sense. A multi-spacecraft system features three additional advantages over a single-spacecraft system: Firstly, by positioning the spacecraft strategically, the blind area which would normally be caused by Solar glare can be minimized: when one spacecraft cannot observe an asteroid because of the relative position of the Sun, another might observe it from the side. Secondly, multiple spacecraft allow for triangulation to determine the position of an asteroid. A single spacecraft can only determine the direction to the NEA in a 2-dimensional fashion, wheras two collaborating spacecraft can directly establish the asteroids position using triangulation. This could shorten the required timeframe for orbit determination. Lastly, although not explored in this work, a multi-spacecraft system could incorporate an advanced search strategy where one or multiple spacecraft take the role of "follow-up" imager: if a possible new NEA is detected, these imagers will be pointed in its direction to achieve swift orbit determination before the target moves out of range again.

At the time of research, no previous analysis had been performed into the general performance of such a system with little constraints in terms or number of spacecraft or their orbits. In particular, this work aims to provide insight into how the number of spacecraft in the system, their orbits, and their payloads, affect the performance of a system and what the optimal values for these parameters are in order to detect as many previously unknown NEAs as possible within a given mission lifetime.

The research is carried out through numerical simulation. A survey model was developed which predicts the resulting detections from a sample population of NEAs and a set of input spacecraft parameters. Firstly, this model is studied using a simplified set of input parameters to obtain a baseline understanding of the individual effect of various parameters. Then, a numerical optimization method is applied to the model to find the optimal values for the various studied parameters.

2. Theoretical models

The work is performed using a model capable of explicitly simulating a multi-spacecraft survey mission. Other research (e.g. Stokes et al. [4], Ramirez Torralba and Heiligers [6]) has previously demonstrated that such simulation tools can be used successfully to study the performance of NEA survey missions. In this section, the theoretical methodology for the various calculation steps is laid out; the practical implementation is laid out in Section 3. Firstly, the generation of a sample asteroid population is discussed in Subsection 2.1. Secondly, methods for estimating the target and background signal when observing these asteroids are detailed in Subsection 2.2. Following this, detector properties of the spacecraft are given in Subsection 2.3, and lastly, in Subsection 2.4, the requirements for detecting and identifying the NEAs are set.

2.1. Population of asteroids

Currently, the most detailed debiased NEA population model is the one developed by Granvik et al. [7]. In this paper, this model is corrected for the fraction of NEAs presumably already identified. For estimation of the latter, the work of Harris and D'Abramo [2] is used. This fraction is shown in terms of absolute magnitude versus frequency in Figure 2. The resulting asteroid distribution used in the work is shown in Figure 3.

Using the model in Figure 3, a representative population of asteroids is generated. For each asteroid a set of Keplerian elements and an absolute magnitude is available. The positions of the asteroids in time are then determined using the assumption of Keplerian motion around the Sun. For each run of the simulation a sample of 1000 asteroids is taken. It was found that increasing the sample size beyond this number did not yield meaningful improvement to the accuracy.

2.2. Target and background signal

To calculate if a spacecraft can detect an asteroid, the signal from the asteroid as observed by the spacecraft is required as well as the background signal in which the target should be detected. Current technology allows for imaging asteroids in both the visual (VIS) as well as the

thermal infrared (TIR) spectrum. The former signal originates in Sunlight reflected off the surface of the asteroid. The latter is the result of the asteroids own thermal emissions and is thus dependent on its temperature. The advantage of detection in the visual spectrum is the higher target signal and the more advanced detector technology; the advantage of thermal infrared is the lower background signal [8].

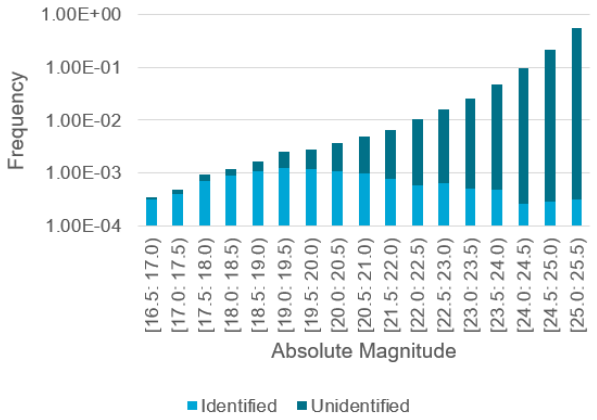

Figure 2: Magnitude-frequency distribution of NEAs according to Granvik et al. [7], including an estimate of the fraction of asteroids already identified, per Harris and D'Abramo [2]. Note that the vertical axis is logarithmic.

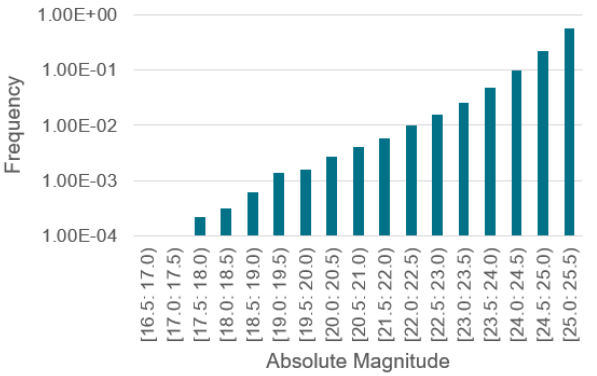

Figure 3: Resulting magnitude-frequency distribution used in this work. Note that the vertical axis is logarithmic.

The signal in the visual spectrum can be obtained straightforwardly. A simple phase equation to obtain the apparent visual magnitude V is given by Stokes et al. [4]:

$$V = \begin{cases} H + 5\log r_t\, d_t - 2.5\log[0.85\Phi_1 + 0.15\Phi_2]; & \beta \geq 60° \\ H + 5\log r_t\, d_t + 5.03 - 10.373\log(\pi - \alpha); & \beta < 60° \end{cases} \quad (1)$$

where:

$$\Phi_1 = e^{-3.33\left(\tan\frac{\alpha}{2}\right)^{0.63}}$$

$$\Phi_2 = e^{-1.87\left(\tan\frac{\alpha}{2}\right)^{1.22}}$$

In Eq. 1, H represents the absolute magnitude, r_t and r_d are the distance from the Sun to the target and the spacecraft to the target, respectively, α is the Solar phase angle and β the Solar elongation.

The signal of the NEA in the thermal infrared spectrum is determined through integration of Planck's law over the visible hemisphere of the asteroid. The temperature of the asteroid can be obtained using the Near-Earth Asteroid Thermal Model (NEATM) as proposed by Harris and Lagerros [9]. By assuming the asteroid to be a spherical, nonrotating body, the temperature T on the asteroids surface is determined as function of the angular distance from the subsolar point ψ as follows:

$$T(\psi) = \begin{cases} T(0)\cos^{1/4}\psi; & \psi < 90° \\ 0; & \psi \geq 90° \end{cases} \quad (2)$$

$$T(0) = [(1 - A_b)F_s/(\eta\epsilon\sigma)]$$

F_s represents the Solar flux, A_b the bond albedo, ε the emissivity and σ is the Stefan-Boltzmann constant. η is a parameter specific to the NEATM, the so-called *beaming parameter*, which is set to 1.22 [9]. From the temperature, the emission f in a bandpass from λ_1 to λ_2 can be calculated using Planck's law:

$$f(T) = \int_{\lambda_1}^{\lambda_2} \frac{2hc^2}{\lambda^5} \frac{1}{e^{hc/(\lambda k_B T)} - 1} \quad (3)$$

where h, k_B and c are the Planck constant, Boltzmann constant, and the speed of light. The signal is then integrated over the visual hemisphere of diameter D with circular coordinates θ and ϕ using an integral well-known from geometry to obtain the target flux F_t:

$$F_t(T) = \frac{D^2}{4} \int_{-\pi/2}^{\pi/2} \int_{-\pi/2}^{\pi/2} f(x) \cos\theta \cos\phi \, d\theta d\phi \quad (4)$$

Similar to the target signal, the background signal must be determined in both the visual and thermal infrared spectrum. For the background signal in the visual light, Roach and Gordon [10] provide tabulated data for the background flux F_b in the visual spectrum at a distance of 1 AU from the Sun. This data is adjusted for the observer's distance from the Sun R according to the correction provided by Leinert et al. [11]:

$$F_b(R) = F_b(1\text{ AU})R^{-2.3} \quad (5)$$

The background signal in the thermal infrared is obtained using the model provided by Kelsall et al. [10]. Based on data from the COBE mission, a model of the distribution and temperature of interplanetary dust is given. Using an equation similar to Eq. 3, the thermal infrared flux from the interplanetary dust can be determined in a given bandpass. Complementary to the contribution of the interplanetary dust, Kelsall et al. [10] provide already processed data of the infrared flux from outside the Solar system.

2.3 Detector properties

With the population, target signal and background signal known, some detector properties are necessary to determine the signal-to-noise ratio (SNR). As optical technology is continuously improving, a set of reference properties given by Stokes et al. [4] is used for the calculation, see Table 1.

Table 1: Hardware properties for space-based survey telescopes [4].

			TIR	VIS
A	Aperture	[m]	0.5	0.5
FoV	Field of view	[deg]	1.7x7.13	10.6x5.3
$\Delta\lambda$	Bandpass	[µm]	6 – 10	0.4 – 1.0
t_i	Integration time	[s]	150	24
Q_e	Quantum efficiency	[%]	65	88
S_D	Dark current	[e-/s]	1	0.00055
S_R	Read noise	[e-]	22	4
k_f	Straddle factor	[-]	0.9	0.9

For thermal infrared detection, a HgCdTe detector is assumed, and for the visual light a silicon CCD [4]. Note that these detectors require a decently sized spacecraft capable of mounting and pointing the telescope, and in the case of the thermal infrared detector, cooling as well. Analysis of space-based surveys using microsatellites is left for further research.

2.4 Detection and identification

The SNR is the ratio between the target signal and the root-sum-square of the noise terms – assuming these terms to be independent [12]:

$$\mathrm{SNR} = \frac{S_t}{\sqrt{S_t + S_b + S_D + S_R^2}} \tag{6}$$

with S_t and S_b the target and background signals obtained from the models described in Subsection 2.2 and S_D and S_R the dark current and readout noise, all in units of e^-. The target signal and the background signal can be calculated from their respective flux using Eqs. 7 and 8.

$$S_t = \frac{1}{hc} A t_i k_f Q_e F_t \tag{7}$$

$$S_b = \frac{1}{hc} A t_i Q_e F_b \tag{8}$$

Detection can be established from the SNR by means of a probabilistic model where an SNR < 1 represents a too high risk of false positives. In that case, detections are rejected. An SNR > 5 represents almost certain detection as false positives are almost impossible. The domain of 1 < SNR < 5 can be modelled through an integrated Gaussian [13].

Of course, detecting an NEA successfully once is insufficient to identify it and determine its orbit. Several consecutive observations which can be *linked* to the same source are required. These observations then allow for orbit determination, e.g. through Gauss' method or solving Lambert's problem. The period in which observations can be successfully linked varies in practice – although timespans up to 90 days result in successful identification in practice [12].

3. Simulation set-up

The theoretical models described in Section 2 have been implemented in a Python simulation program. A schematic is shown is Figure 4. The simulation program can evaluate the performance of a survey from only the properties of the detector (see Subsection 2.3), the orbital elements of the spacecraft, and the time of the survey. Then at each timestep (based on the survey cadence, see Subsection 3.1), it is evaluated whether the spacecraft are capable of detecting any of the asteroids. Successful detections are counted, and a sufficient number of detections within a 90-day period will lead to the asteroid being identified. This process is then repeated for a mission lifetime of 5 years. A schematic of the simulation can be seen in Figure 3. Where necessary, random number generation is carried out using the *numpy* package [14], with the initial seed value set arbitrarily to 9 at the start of each run.

3.1 Survey cadence

An assumption is made about the survey cadence in order to determine the simulation timestep: in reality, a spacecraft would need to image one area of the sky, and then move on to the next, until it has covered the search area completely. The time it takes to complete a full imaging of the sky is the survey cadence. However, such a way of modelling represents a too high computational load. Therefore, the assumption is made that all observations in one cycle of imaging the sky are made simultaneously, rather than spaced apart slightly in time,

while still imaging each part of the sky an equal number of times. The effect of this assumption on the computed survey completeness is minor [15]. The timestep for the simulation Δt is thus the time required for a spacecraft to image the entire sky. This can be calculated according to:

$$\Delta t = \frac{360^2}{\pi} / \, FoV \cdot (t_i + t_s) \tag{9}$$

Where the slew time t_s is assumed to be 30 seconds. This results in a survey cadence of 21 days for a system with a thermal infrared detector, and 2 days for a system with a visual light detector.

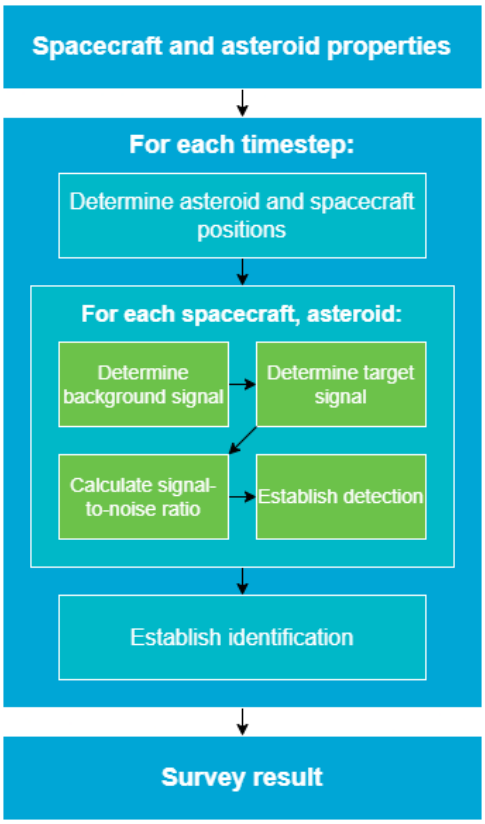

Figure 4: Overview of the simulation architecture.

3.2 Orbital mechanics

The position of the asteroids and spacecraft at each timestep is determined assuming Keplerian motion of both the asteroids and the spacecraft around the Sun. Thus, no numerical integration or propagation of the orbit is required. The transcendental Kepler equation was solved using the numerical method proposed by Murison [16]. MJD2000 is taken as epoch for every simulation, although no significant deviation in results was found when starting the survey at a different time due to the radial symmetry of the population [7].

3.3 Implementation of target and background signal

The signal of the target in the visual light spectrum is directly implemented using Eqs. 1 and 2. The signal in the thermal infrared spectrum however requires a triple integration to obtain. This integration is performed numerically using several assumptions necessary to reduce the computational effort.

Firstly, the integration over the bandpass $\Delta\lambda$ is approximated by taking the average of the start and the end of the bandpass, as Planck's law $B(\lambda, T)$ is a relatively smooth function:

$$\int_{6\mu m}^{10\mu m} B(\lambda, T)\mathrm{d}\lambda \approx \frac{1}{2}[B(6\mu m, T) + B(10\mu m, T)]\Delta\lambda \tag{10}$$

Furthermore, the double integration in Eq. 4 is performed using a Riemann sum, using the midpoint rule, and an interval of $\pi/4$ for both directions. This results in a manageable total of 16 evaluations per calculation. It was found that the error with respect to a very precise integration is in the order of 1% [15].

Implementation of the background signal is carried out through tabulation of the sources laid out in Subsection 2.2. For the signal in the visual spectrum, the data is provided in already tabulated form by Roach and Gordon [10]. The background signal in the thermal infrared spectrum is tabulated in two steps: firstly, the portion of the signal originating from outside the Solar system is provided by Kelsall et al. [17] and this is loaded into the model directly. The portion of the signal originating from interplanetary dust and the Sun is found by implementation of the model as described in [17]. The resulting signal is calculated for a range of reference values and then tabulated and saved.

3.4 Optimization

As alluded to previously, the objective of the proposed mission is to identify as many unidentified NEAs as possible. For this, the survey completeness C is defined as the ratio of identified NEAs n_{id} to total NEAs n_t:

$$C = \frac{n_{id}}{n_t} \tag{11}$$

The objective of the optimization problem is thus to find a set of spacecraft parameters which leads to the highest achievable survey completeness. As explained in Section 1, the possibility of triangulation of target asteroids is to be taken into account. To ensure that this is possible, the minimum angular separation between the spacecraft is set (arbitrarily) to 0.3 rad ≈ 17.2 deg. In addition, as an increase in the number of spacecraft should logically never lead to a reduction in the

performance, the problem is evaluated separately for differing numbers of spacecraft. The process for this is described in Subsection 3.5.

Typical optimization methods are unsuitable for solving the posed problem because they either require knowledge of some analytical properties of the system, such as the gradient, or require evaluation of a very large number of points which is infeasible due to the associated computational load. Therefore, the method of *surrogate optimization* is applied in this work. In this method, a different function, the *surrogate*, which is straightforward to optimize, is fitted to the model. Initially, a few randomly selected points are evaluated. Then, using the surrogate model, the optimal point is estimated. This point is then evaluated in the simulation model, and the output is used to update the surrogate. This process is repeated until the solution converges [18]. Several surrogate functions were considered: tree-based regression models, gradient-boosted trees [19], random optimization (i.e. surrogate function gives equal probability to all points), and a Gaussian process [20]. The latter was found to provide the best convergence for the optimization process. The optimization algorithm was implemented by means of the *Scikit-Optimize* library [21].

Before applying the optimization scheme, a grid search is employed to obtain initial insights in the effect of the different design parameters in the problem. The results of this grid search then also allow a reduction of the design space. For these initial runs, it is assumed that the spacecraft are co-orbital, and that the angular distance between all neighbouring spacecraft is equal. The mean anomaly at epoch M of spacecraft n out of N can thus be expressed as a function of the *inter-spacecraft spread* ΔM:

$$M_n = (n-1)\Delta M - \frac{N-1}{2}\Delta M \tag{12}$$

As mentioned previously, the minimum value for ΔM was set to 0.3 rad ≈ 17.2 deg, and its maximum value is $2\pi/N$, at which point the spacecraft are spread evenly over the orbit. Thus, the parameter space is reduced to the following parameters:

- The number of spacecraft
- Their payload
- The semi-major axis of the orbit
- The eccentricity of the orbit
- The inter-spacecraft spread

4. Grid search results

As described in the previous section, a grid search is first performed to evaluate some properties of the model before applying the optimization scheme. Firstly, in Subsection 4.1, the effect of the semi-major axis, eccentricity, and inter-spacecraft spread for co-orbital configurations is discussed. Then, the effect of the number of spacecraft and their payload is discussed in Subsection 4.2 and 4.3, respectively. Lastly, in Subsection 4.4, a hypothesis is presented on the driver of the observed performance. The optimization results are discussed in Section 5.

4.1 Orbital elements

In Figure 5 the modelled survey completeness is shown for a system of 1-5 spacecraft imaging in the visual light and thermal infrared spectrum, as a function of their semi-major axis around the Sun. The orbital eccentricity and the inter-spacecraft spread are optimized through a grid search for each case. It can be seen firstly that there is an optimum for the semi-major axis, and secondly, that the function is quite flat around the optimum; solutions with a semi-major axis up to 0.1 AU away from the optimum result in similar performance. Thus, these solutions can be considered in mission design.

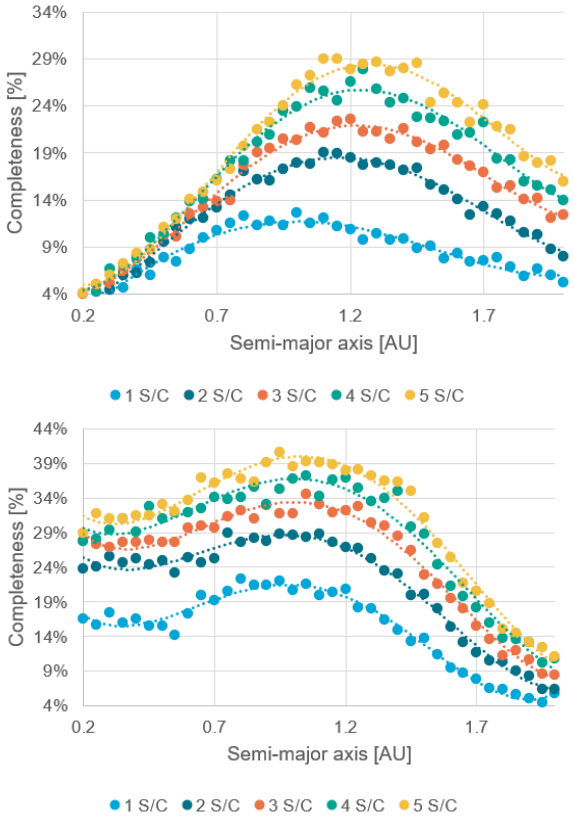

Figure 5: Expected survey performance as a function of semi-major axis in the visual light (top) and thermal infrared (bottom).

Secondly, in Figure 6 the relationship between the optimal semi-major axis and the number of spacecraft is shown. Ten subsequent runs with different population samples are carried out to estimate the uncertainty: The

initial *np.random.seed* value is set to 9, then a population of 1000 is sampled from the model presented in Subsection 2.1, the model is evaluated on this population, and then a new population is drawn using the current state of *np.random* (i.e., not reseeding the generator using a new *np.random.seed* call). Although it is observed that the uncertainty is quite high due to the flatness of the function around the optimum, there is a clear upward trend in the semi-major axis for increasing numbers of spacecraft imaging in both the visual light as well as the thermal infrared spectrum.

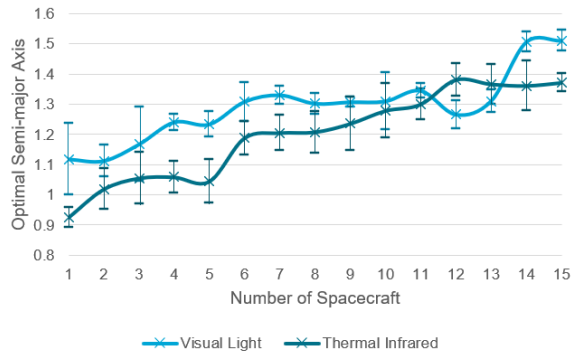

Figure 6: Optimal semi-major axis as a function of the number of spacecraft. Standard deviation is obtained from sampling 10 runs with different population samples.

Results for the second orbital element, the eccentricity, can be seen in Figure 7. These solutions are optimized for semi-major axis and inter-spacecraft spread using a grid search. Clearly, non-circular orbits show no improvement in performance, and for high eccentricities are even very detrimental.

Lastly, the expected survey completeness as a function of the inter-spacecraft spread, the angular separation between the spacecraft, is shown in Figure 8. As before, the other two parameters in these solutions are optimized using a grid search. From the results, it can be seen that a system with the spacecraft spread out as much as possible over the orbit is expected to give the best performance in all cases. Although it might appear that some periodicity is present in the results, notably for the 1 and 2 spacecraft cases, no statistically significant signal is present; the occurrence is incidental.

Thus, when only considering the survey performance in a co-orbital configuration, the best configuration for a system of spacecraft is to position the spacecraft in a circular orbit, spread out as much as possible from each other. The optimal value for the semi-major axis is dependent on the number of spacecraft but allows for some leeway around the optimum.

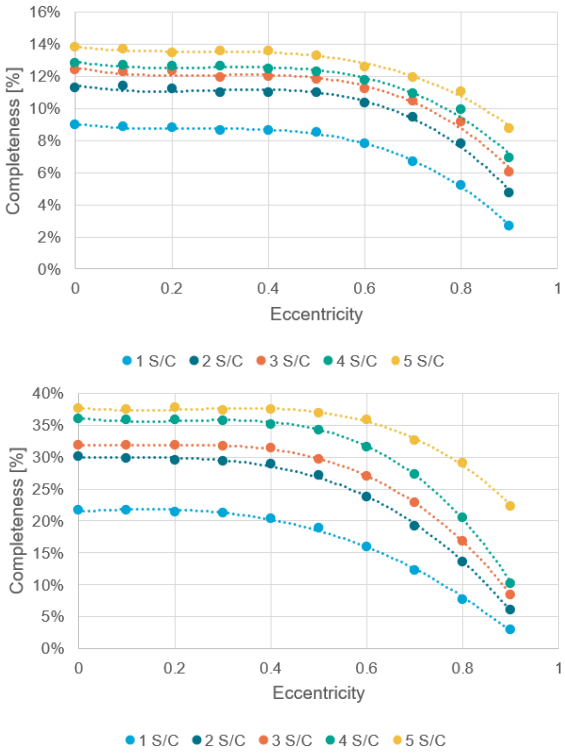

Figure 7: Expected survey performance as a function of eccentricity in the visual light (top) and thermal infrared (bottom).

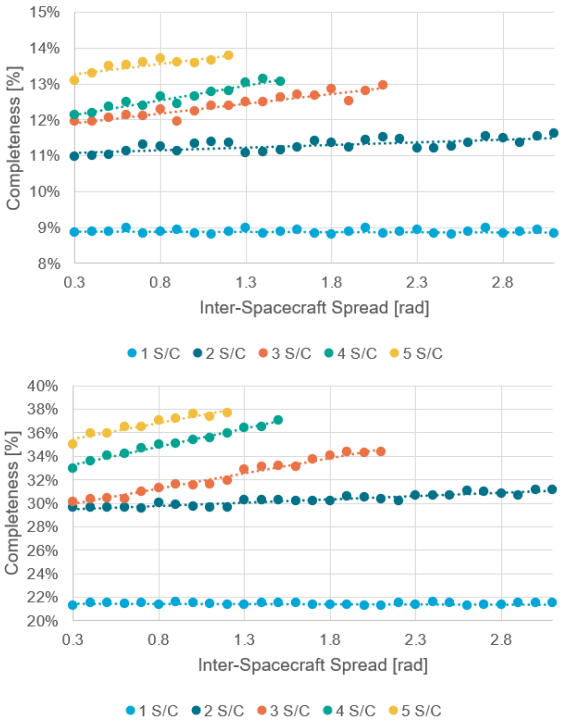

Figure 8: Expected survey performance as a function of inter-spacecraft spread in the visual light (top) and thermal infrared (bottom).

4.2 Number of spacecraft

As mentioned previously, increasing the number of spacecraft will, at worst, leave the performance of the system unchanged. However, in practice there will be other constraints - primarily economical in nature - which limit the number of spacecraft available for a given mission. Such a comparison is thus essential for determining the cost-benefit relationship of a multi-spacecraft NEA survey mission.

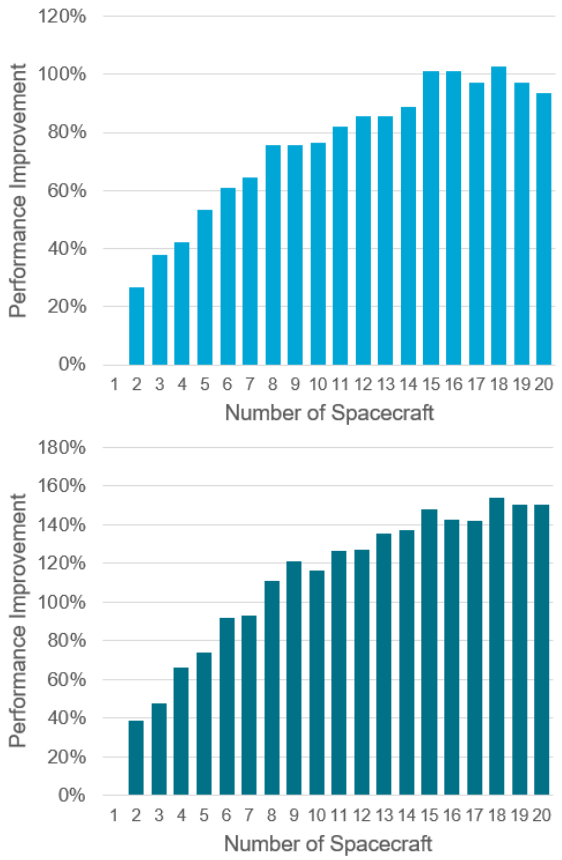

Figure 9: Expected performance in terms of survey completeness relative to a 1-spacecraft system in the visual light (top) and thermal infrared (bottom).

Using the optimal positioning obtained in Subsection 4.1, the performance for missions of 1 to 20 spacecraft is evaluated. The expected survey completeness relative to the one expected from a 1-spacecraft mission is shown in Figure 9. It is apparent that increasing the number of spacecraft indeed increases the performance of the system. Especially the addition of a second spacecraft yields a large relative performance increase of 25% for visual light and 40% for thermal infrared imaging systems. However, it is also apparent here that there is very strong diminishing returns present. Larger numbers of spacecraft yield relative performance increases in the order of a few percent. Clearly, achieving a survey completeness close to 100% is not feasible with a multi-spacecraft system utilizing present-day imaging systems. Lastly, it should be noted that the relative increase is significantly higher for thermal infrared systems than for visual light systems. Previous work (Stokes et al. [4], Ramirez Torralba and Heiligers [6]) has shown that thermal infrared systems are superior in single spacecraft missions; this finding thus suggests that thermal infrared systems will be superior in multi-spacecraft systems as well.

4.3 Payload

Although it could be concluded that thermal infrared systems will provide better performance in a system which only features one type of detector, this conclusion does not necessarily extend to systems with a combination of the two payload types. Systems of two and four spacecraft are evaluated for all combinations of VIS and TIR payloads; firstly, to identify if any synergistic effect between the payloads is present, and secondly to see if presence of VIS detectors in the system leads to an increase in performance on shorter timescales due to their faster cadence.

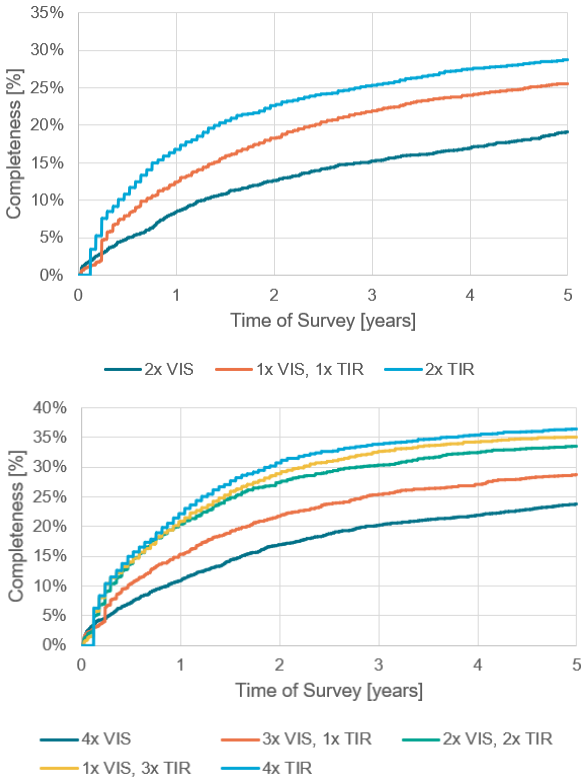

Figure 10: Survey performance over time for mixed payload configurations in a system of two (top) and four (bottom) spacecraft.

Figure 10 shows the expected performance over time for these systems. For a typical mission lifetime of 5

years, the best performance is achieved with a purely thermal infrared system. On very short timescales the visual light systems outperform, but this is only since any system requires at least three separate observations to determine any orbit, and thus the thermal infrared system only obtains its first detections after 42 days, compared to 4 days for the visual light system.

4.4 Explanation of observed phenomena.

Following the analysis presented in Subsections 4.1 – 4.3, we propose a theory on what exactly drives the survey performance. The hypothesized mechanism driving performance is the volume of space in which the system can effectively detect NEAs. Implicitly, this assumes the population of NEAs is distributed evenly throughout space. In the angular direction, this is approximately true. However, in the radial direction, this does not hold. Thus, these findings can only be utilized to qualitatively explain the phenomena observed in the previous Subsections; they cannot be used for quantitative performance prediction or optimization.

Successful identification of an NEA requires subsequent detections, and these detections require a high enough signal-to-noise ratio to achieve. Therefore, spacecraft should be positioned to achieve a sufficient SNR on as many NEAs as possible. From the observation model, the limiting absolute magnitude at which an SNR of 5 can be achieved by the system for an NEA at a given location can be calculated iteratively. Performing this calculation for a representative set of points yields a diagram as can be seen in Figure 11. Note that, as NEAs are mostly concentrated around the ecliptic plane, only the coverage area in the ecliptic plane is considered for simplicity. In Figure 11, a few things can be seen: The Sun is shown in yellow in the centre. The spacecraft and its orbit are both shown in red. Close to the spacecraft, opposite the Sun, the limiting magnitude is high: very small NEAs can be detected. Conversely, when imaging towards the Sun, no NEAs will be detected. In the volume

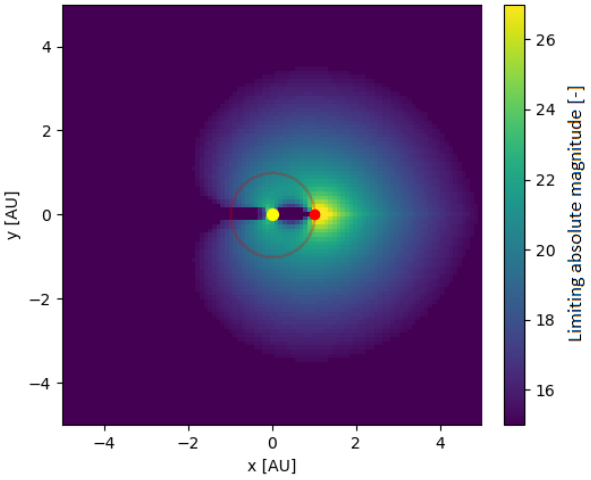

Figure 11: Example of coverage diagram for a spacecraft in a 1.0 AU circular orbit. The (x, y)-plane coincides with the ecliptic plane.

of space surrounding the spacecraft, the limiting magnitude decreases (NEAs have to be larger to be detected) as the distance to the spacecraft and the Solar phase angle become less favourable.

4.4.1 Number of spacecraft

Figure 12 shows the coverage diagram for a system of 1, 3 and 5 spacecraft. A larger volume of space is covered by a larger number of spacecraft, and the spacecraft are capable of covering each other's blind spots towards the Sun. Thus, a performance increase is expected, and observed in Figure 9. However, as the number of spacecraft increases, an overlap arises between the coverage area and as such diminishing returns are observed. However, this overlap mainly presents itself for larger NEAs, and the effect is thus expected to be smaller for smaller NEAs. This is further examined in Subsection 4.6.

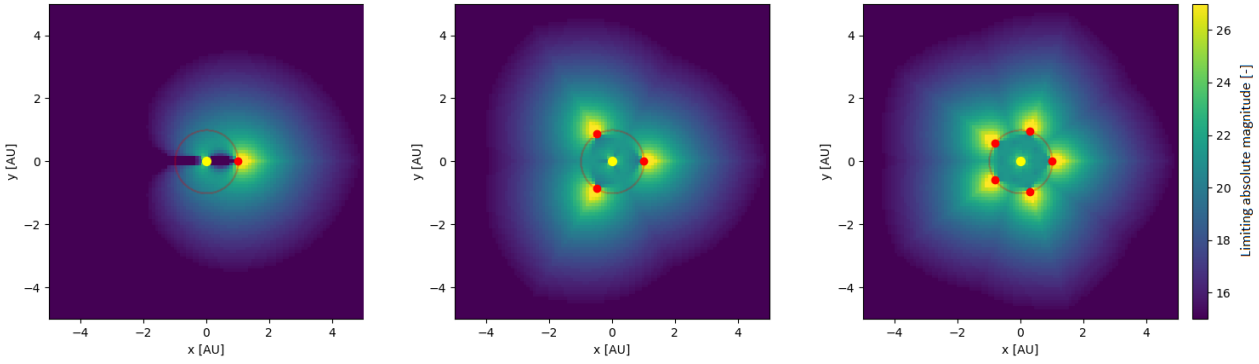

Figure 12: Coverage diagram for a system of 1, 3 and 5 spacecraft, spread evenly over the orbit. The (x, y)-plane coincides with the ecliptic plane.

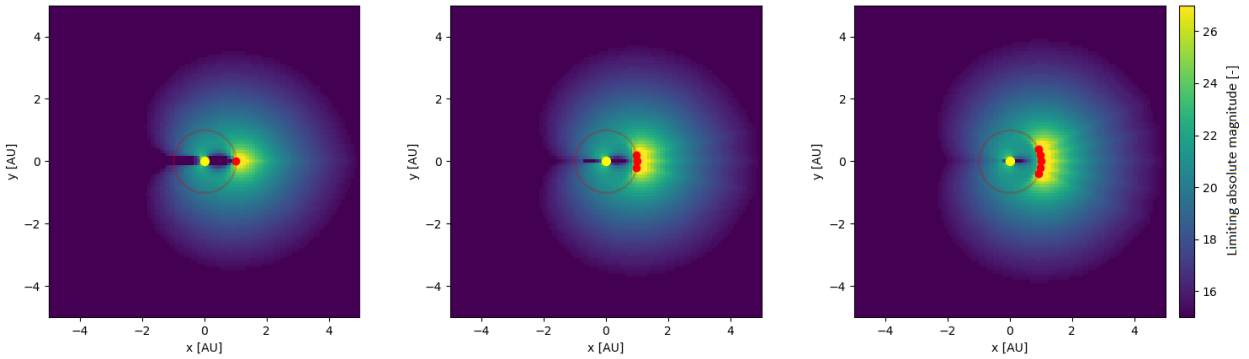

Figure 13: Coverage diagram for a system of 1, 3 and 5 spacecraft, grouped together with minimal inter-spacecraft spread. The (x, y)-plane coincides with the ecliptic plane.

4.4.2. Inter-spacecraft spread

Figure 13 shows the coverage diagram for a system of 1, 3, and 5 spacecraft at a small inter-spacecraft distance. Comparing this diagram to the situation in Figure 12, it becomes clear that the observed overlap is much more present in the low spread case. As such, a high inter-spacecraft spread is expected to perform best, as also observed in Figure 8.

4.4.3. Semi-major axis

Figure 14 shows the coverage diagram for a system of 5 and 15 spacecraft, the latter of which in an orbit with a semi-major axis of 1.0 AU and 1.5 AU. Here, it is observed that for high numbers of spacecraft, the overlap can be decreased by increasing the semi-major axis, where the higher number of spacecraft still allows for efficiently imaging the sky although individual spacecraft might not be in their optimal position. This explains why the optimal semi-major axis increases for increasing numbers of spacecraft, as observed in Figure 6.

4.4.4 Differing semi-major axes

From the previous examples, it might be tempting to conclude that a non-co-orbital configuration should be superior to a co-orbital configuration. After all, placing the spacecraft in different orbits allows for reducing the overlap (and thus increasing the coverage area) by more than is possible in a co-orbital configuration. However, this is not the case in practice, which is illustrated in Figure 15. Initially, it appears as if moving the spacecraft from the configuration shown in the left figure to the one in the middle will improve the coverage. However, differing semi-major axes imply different orbital velocities, and as such the inter-spacecraft spread quickly drops over time and configurations such as the one shown on in the figure on the right arise. In this configuration, there is both significant overlap between the spacecraft coverage areas, and there are blind spots present. Therefore, it is hypothesized that non-co-orbital configurations will not outperform the co-orbital solutions. This latter hypothesis will be tested in Section 5.

5. Optimization

As explained previously, optimization of the problem is difficult: the problem is computationally expensive and does not offer easy ways op optimization, the solution is locally insensitive to changes in the input, and the complex non-linearity in the model results in a

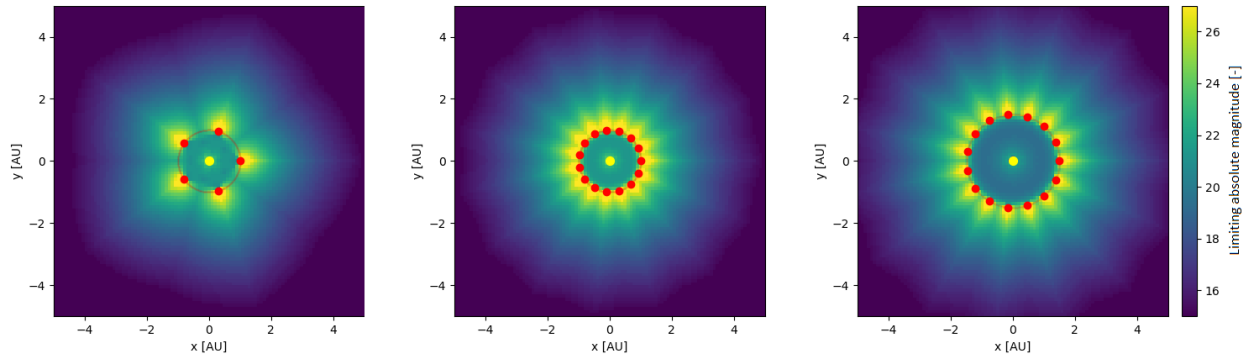

Figure 14: Coverage diagram for a system of 5 and 15 spacecraft, the latter at both 1.0AU and 1.5AU semi-major axis. The (x, y)-plane coincides with the ecliptic plane.

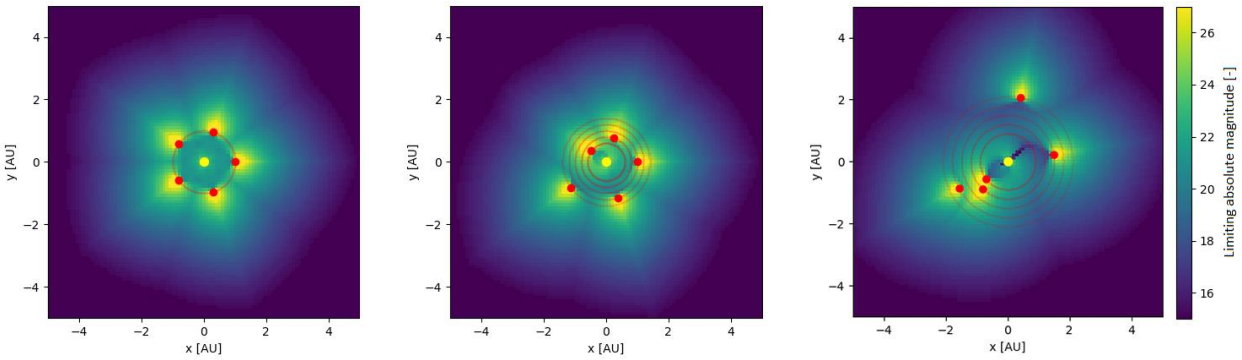

Figure 15: Coverage diagram for 5 spacecraft with differing semi-major axes. In the first figure, all 5 spacecraft are in a 1.0 AU orbit. In the middle and right figures, the spacecraft are in orbits of 0.6, 0.8, 1.0, 1.2 and 1.4 AU. The second and third figures are generated at t=0 and t=1 year, respectively. The (x, y)-plane coincides with the ecliptic plane.

considerable amount of variance in the results. Three different optimization cases are examined to not only determine the optimal solution, but also to evaluate the accuracy of the optimization process itself. The first optimization case corresponds to the optimal solution found in Section 4: spacecraft spread evenly over the orbit, in a single circular orbit. For the second case a non-co-orbital configuration in considered, however with the spacecraft still constrained to circular orbits. Lastly, a non-circular, non-co-orbital configuration is evaluated. According to the hypothesis in Subsection 4.4, the non-co-orbital configurations are not expected to outperform the co-orbital solution.

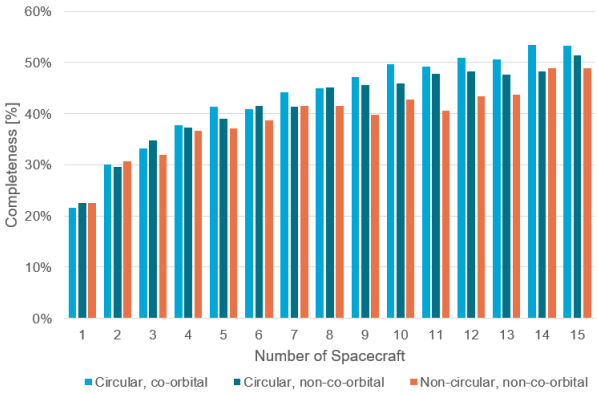

Figure 16: Resulting performance after optimization for 1-15 spacecraft, for all three optimization cases.

The expected performance for the three cases as a function of the number of spacecraft is shown in Figure 16. Indeed, no outperformance is observed for the non-co-orbital configurations. However, unexpectedly, the non-co-orbital cases systematically underperform for a higher number of spacecraft. This is illogical, as the constraints on the optimizer permit producing the same solution as the co-orbital optimization case. For this reason, the difference between the performance predicted by the optimizer, and the performance achieved on a validation dataset, i.e., the overfit, is analysed in Figure 17. Clearly, the optimizer shows more overfitting for the non-co-orbital configuration. This indicates a shortcoming in the optimization process. However, even for lower numbers of spacecraft, no solutions are found at all which significantly outperform the co-orbital configuration. For this reason, combined with the findings from Subsection 4.4, it is expected that the co-orbital, circular solution with the spacecraft spread out evenly over the orbit is the optimal solution. However, the problems in the optimization preclude drawing a definitive conclusion on this fact.

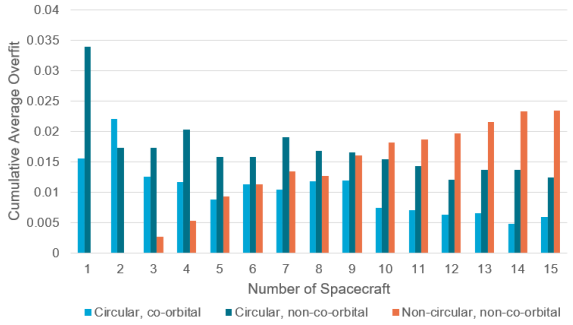

Figure 17: Comparison of the optimizer overfit.

4.6 Expected performance

For consideration in future missions, it is important to assess what performance can be expected from a multi-spacecraft NEA survey system. Figure 18 shows the expected completeness for 1-6 spacecraft operating in the thermal infrared spectrum, in the circular co-orbital configuration detailed previously, with the semi-major axis optimized using the method of surrogate optimization. The completeness is shown as a function of the absolute magnitude of the NEA. Current completeness (from [2]) and expected completeness with current efforts (from [4]) are also shown. Despite the

diminishing returns observed previously, there is still some increase in performance mainly at smaller sizes for higher numbers of spacecraft. Thus, the ideal number of spacecraft can be determined based on the objective of the mission.

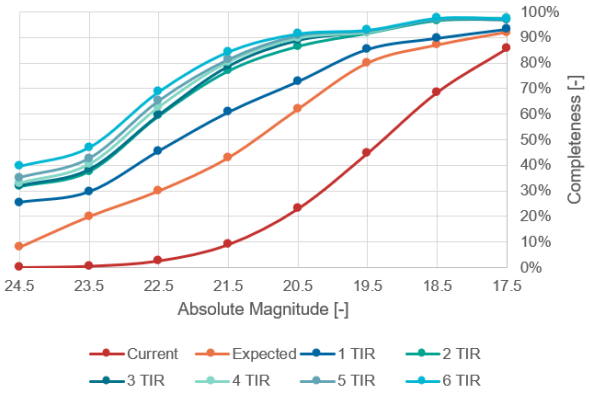

Figure 18: Expected completeness as a function of absolute magnitude.

Lastly, Table 2 shows an overview of the optimal semi-major axis and the expected survey completeness for 1 - 6 spacecraft in a circular co-orbital configuration, spread out as much as possible over the orbit. These values are found to be consistent across both the initial grid search, and the subsequent optimization efforts.

Table 2: Optimal semi-major axes and expected completeness.

Spacecraft	Semi-major axis	Completeness
1	0.90 – 1.00 AU	22%
2	0.95 – 1.05 AU	30%
3	1.00 – 1.10 AU	34%
4	1.00 – 1.10 AU	37%
5	1.05 – 1.15 AU	40%
6	1.05 – 1.15 AU	42%

6. Conclusions

This paper has presented research that aims to provide a baseline for the behaviour and expected performance of potential future multi-spacecraft NEA survey missions. Advantages of such a multi-spacecraft system over a system comprising a single spacecraft are a reduction in the blind spots due to Solar interference, faster orbit determination through triangulation, and the possibility for application of advanced search strategies, although the latter is left for future research. Through development of a simulation model, it was found that the best performance can be achieved by placing all spacecraft in a circular, co-orbital configuration, with the semi-major axis dependent on the number of spacecraft. Furthermore, all spacecraft should utilize thermal infrared detectors rather than detectors operating in the visual spectrum, and they should be spread out over the orbit as much as possible. With such a system, it is expected that in 5 years 30% of unknown NEAs can be identified with a 2-spacecraft system, up to 42% for a 6-spacecraft system, with performance increasing for even larger numbers of spacecraft, although with significant diminishing returns.

Lastly, it is noted that these conclusions are not without caveat. Positioning and operating spacecraft in such a configuration is hardly a trivial effort from an engineering standpoint. Furthermore, issues with the optimization algorithm preclude drawing a definite conclusion on the performance of non-co-orbital configurations, although our results do support the finding that a circular, co-orbital arrangement should provide the best results as it covers the search volume in the most effective manner.

References

[1] Morrison, D. et al. (1992). *The Spaceguard survey report* (tech. rep.). NASA/JPL. Retrieved from https://archive.org/details/nasa_techdoc_19920025001/mode/2up

[2] Harris, A., & D'Abramo, G. (2015). *The population of near-Earth asteroids*. Icarus, 257.

[3] Harris, A. (2008). *What Spaceguard did*. Nature, 453.

[4] Stokes, G. H. et al. (2017). *Update to determine the feasibility of enhancing the search and charactization of NEOs* (tech. rep.). NASA Science Mission Directorate.

[5] Mainzer, A. et al. (2014). *Initial performance of the NEOWISE reactivation mission*. The Astrophysics Journal, 792.

[6] Ramirez Torralba, O. & Heiligers, M.J. (2020). *Mission analysis of space-based telescopes to detect impacting near-Earth objects*. AAS/AIAA Astrodynamics Specialist Conference 2020.

[7] Granvik, M. et al. (2018). *Debiased orbit and absolute-magnitude distributions for near-Earth objects*. Icarus, 312.

[8] Stokes, G. H. et al. (2003). *Study to determine the feasibility of extending the search for near-Earth objects to smaller limiting diameters* (tech. rep.). NASA Science Mission Directorate.

[9] Harris, A., & Lagerros, J. (2002). *Asteroids in the thermal infrared.* Asteroids III.

[10] Roach, F. E., & Gordon, J. L. (1973). *The light of the night sky.* Geophysics and Astrophysics Monographs.

[11] Leinert, C. et al. (1998). *The 1997 reference of diffuse night sky brightness*. Astronomy and Astrophysics Supplement Series, 127.

[12] Adams, E. et al. (2018). *Analysis of alternatives for near Earth object detection, tracking and charactization.* (tech. rep.). John Hopkins Applied Physics Laboratory.

[13] Meyzonnette, J.-L. (2007). *Probability of detection and minimal value of SNR* in *Semiconductor sensors and application*. Institut d'Optique Graduate School
[14] *Numpy*. https://numpy.org/
[15] Vermeulen, J. G. P. (2022). *Identification of near-Earth asteroids using multi-spacecraft systems* (Master's thesis). Delft University of Technology.
[16] Murison, M. (2006). *A practical method for solving the Kepler equation*. U.S. Naval Observatory.
[17] Kelsall, T. et al. (1998). *The COBE diffuse infrared background experiment search for the infrared background. II. Model of the interplanetary dust cloud.* The Astrophysics Journal, 508.
[18] Queipo, N.V. (2005). *Surrogate-based analysis and optimization*. Progress in Aerospace Sciences, 41.
[19] Geron, A. (2019). *Hands-on machine learning with Scikit-learn, Keras, and Tensorflow*. O'Reilly.
[20] Mockus, J. (2012). *Bayesian approach to global optimization: theory and applications.* Kluwer Academic.
[21] *Scikit-optimize*. https://pypi.org/project/scikit-optimize/